

Macroscale-area patterning of three-dimensional DNA-programmable frameworks

Received: 6 June 2024

Accepted: 18 March 2025

Published online: 04 April 2025



Feiyue Teng¹, Honghu Zhang², Dmytro Nykypanchuk¹, Ruipeng Li², Lin Yang², Nikhil Tiwale¹, Zhaoyi Xi¹, Mingzhao Liu¹, Mingxin He³, Shuai Zhang^{4,5} & Oleg Gang^{1,3,6,7} ✉

DNA, owing to its adaptable structure and sequence-prescribed interactions, provides a versatile molecular tool to program the assembly of organized three-dimensional (3D) nanostructures with precisely incorporated inorganic and biomolecular nanoscale components. While such programmability allows for self-assembly of lattices with diverse symmetries, there is an increasing need to integrate them onto planar substrates for their translation into applications. In this study, we develop an approach for the growth of 3D DNA-programmable frameworks on arbitrarily patterned silicon wafers and metal oxide surfaces, as well as study the leading effects controlling these processes. We achieve the selective growth of DNA origami superlattices into customized surface patterns with feature sizes in the tens of microns across macroscale areas using polymer templates patterned by electron-beam lithography. We uncover the correlation between assembly conditions and superlattice orientations on surfaces, lattice domain sizes, twinning, and surface coverage. The demonstrated approach opens possibilities for bridging self-assembly with traditional top-down nanofabrication for creating engineered 3D nanoscale materials over macroscopic areas with nano- and micro-scale controls.

DNA-programmable superlattices refer to nanoscale structures wherein DNA molecules and nanostructures drive the assembly of nano-objects into ordered, periodic arrangement. Such lattices and complex designed arrangements are envisioned to enable diverse optical, electronic, and biological properties of the nanomaterials through precise structural control, emergent collective effects, and large-scale integration^{1–9}. For 3D superlattices, the integration of superlattices with planar substrates is particularly important for manipulating their lattice growth via interfacial crystallization¹⁰ and for the incorporation of lattices into devices¹¹. Guiding DNA-programmed nanostructures to specific substrate locations

typically requires a site-specific interaction between the DNA nanostructure and the surface. Using surfaces patterned with distinctive affinities can ensure that the nanostructures selectively adhere to predetermined areas, allowing for predefined placement. The combination of DNA-programmable self-assembly and lithography methods can leverage the strengths of both methods to create complex and precisely engineered structures by guiding crystallization processes^{12,13}, thus enabling the fabrication of multi-scale structures using DNA-programmable assembly strategy.

Previous studies utilized surface patterning to place individual DNA origami on a pattern, where cation-mediated interactions

¹Center for Functional Nanomaterials, Brookhaven National Laboratory, Upton, NY, USA. ²National Synchrotron Light Source II, Brookhaven National Laboratory, Upton, NY, USA. ³Department of Chemical Engineering, Columbia University, New York, NY, USA. ⁴Physical Sciences Division, Pacific Northwest National Laboratory, Richland, WA, USA. ⁵Department of Materials Science and Engineering, University of Washington, Seattle, WA, USA. ⁶Department of Applied Physics and Applied Mathematics, Columbia University, New York, NY, USA. ⁷Center for Nanomedicine, Institute for Basic Science (IBS), Seoul, Republic of Korea. ✉e-mail: og2226@columbia.edu

between origami and silicon oxide^{14–17}, silicon nitride^{18,19}, and glass²⁰ surfaces were used. Covalent coupling²¹ and gold-thiol²² binding were also demonstrated for attaching single DNA origami onto surfaces. The immobilization of 2D DNA-origami lattices on homogenous surfaces was studied, with the most commonly utilized mica surfaces^{23–29} and lipid bilayers on mica^{30,31}. Recently, large-area DNA origami lattices were also successfully assembled on silicon surfaces^{32,33} with random placement of lattice domains. Interest in utilizing DNA lattices for bio-imaging also resulted in their recent integration with Cryo-TEM grids³⁴. In parallel, the assembly of DNA-functionalized nanoparticles on planar surfaces was explored, including polycrystalline films^{35–37}, responsive films^{38,39}, and single-crystal Winterbottom constructions^{10,11,40}. By combining lithographically defined gold patterns coated with thiolated DNA strands, both DNA-functionalized superlattice films⁴¹ and single-crystals^{42–44} were formed at the specific pattern-define locations. Recently, a protein-assisted approach was demonstrated for patterning different DNA origami species⁴⁵.

DNA origami lattices, or so-called frameworks, offer a platform approach for the self-assembly of 3D lattice due to the ability to control lattice type via directional bonds and integrate diverse types of inorganic and biomolecular nanocomponents^{5,46}. This allows the rationalization of nanomaterial assembly by considerably decoupling the assembly process from the specific details of nanocomponents. Moreover, inorganic templating further provides a path for creating inorganic frameworks from diverse material types based on the DNA origami lattice architecture^{7,46–49}. By integrating these 3D lattices of DNA frames on patterned surfaces, the assembly process can lead to the fabrication of hierarchical structures across multiple scales and device integration. Patterned surfaces are crucial for forming controllable 3D DNA framework arrangements at larger scales. This ability to adapt to various substrate types with distinct chemical compositions is important for translating advances in DNA-programmable 3D assembly to applications. Since the resulting interfacial crystallization process is sensitive to the interactions between nanocomponents and the surfaces, adapting it to different surfaces requires customization and optimization. A universal method for growing 3D DNA-programmed superlattices on various types of surfaces would facilitate the integration of bottom-up and top-down fabrication methods. Therefore, understanding the key factors influencing the self-assembly process at liquid-solid interfaces is required. To tackle this challenge, we utilize DNA origami frame absorption on charged surfaces to guide DNA-programmed interfacial crystallization of DNA origami superlattices. The non-specific interactions between nanocomponents and surfaces offer several advantages, including simplified requirements for chemical grafting of DNA to surfaces, enhanced compatibility with potential semiconductor or electronic devices, and fewer processing steps.

In this work, we demonstrate an approach for directing the assembly of DNA-frame programmable 3D superlattices to specific locations on planar surfaces over macroscopic areas. We identify the factors controlling crystal orientations, sizes, twinning, and surface coverage. The approach is applicable to a variety of surfaces, including silicon oxide (SiO₂) surfaces on a silicon wafer, and metal oxide surfaces such as aluminum oxide (Al₂O₃), titanium dioxide (TiO₂), and zinc oxide (ZnO). DNA frames are immobilized on oxide surfaces through electrostatic interactions, and then these surface-bound frames promote interfacial nucleation and crystallization of 3D superlattices. We further extend this methodology to generate surface-patterned arrays with frame-encapsulated nano-cargos, including nanoparticles and proteins. We demonstrate our approach for creating 3D superlattices in the form of regular and arbitrary patterns with tens of microns features over macroscale (millimeters) areas and investigate the key factors affecting crystallization at the patterned surfaces.

We hypothesize that directing the assembly of 3D DNA frame superlattices on planar substrates could be achieved by strategically depositing an initial layer of DNA frames on the designated areas of

surfaces. This approach allows guiding superlattice growth on the patterned areas by the initial layer of adsorbed DNA frames due to their affinity to these areas. Tuning the composition of the DNA frames in this initial layer affects the subsequent assembly process. For a frame-surface affinity, we use the adhesion of DNA frames to hydrophilic oxide surfaces through divalent cation (Mg²⁺) bridging that links the negatively charged surfaces with the negatively charged DNA backbones and leads to the formation of the initial frame layer. The fact that the interaction between the first layer of DNA frames and surfaces is non-specific makes it possible to adapt this approach to various oxide surfaces.

Achieving precise control over the assembly process at specific locations on a substrate requires creating surfaces with surface-defined localized distinctive interactions. This involves pretreating the substrate to enhance frame-surface affinity and passivate areas where the assembly is not desired. In our design, lithographically patterned polyethylene glycol (PEG) hydrogels are used as surface templating media to define active areas for the formation of a single layer of DNA frames through electron beam patterning. This allows us to guide the interfacial crystallization to specific locations on surfaces. The schematic of the patterning and assembly of 3D DNA frame superlattices on patterned substrates is shown in Fig. 1a (for a comprehensive description, refer to the Methods section, and for detailed schematics, see Supplementary Figs. S1 and S3).

First, a thin layer of PEG was spin-cast onto silicon wafers with an oxide layer (SiO₂, Al₂O₃, TiO₂, ZnO) that was pretreated with oxygen plasma. Second, electron-beam lithography (EBL) was used to define a pattern on the PEG layer^{50,51}, where the electron beam induces polymer crosslinking within the exposed areas. The PEG in the non-irradiated area was then dissolved in water, resulting in an array of microwells that revealed the substrate. These microwells have a depth of approximately 50 nm when dry, which increases to about 350 nm upon hydration, as probed by the AFM measurements (Supplementary Fig. S14). Third, the exposed oxide surface at the bottom of each microwell was functionalized with DNA frames by incubating the substrates with the corresponding DNA frame solution, where Mg²⁺ cations bridge a negatively charged surface generated by oxygen plasma treatment and a negatively charged DNA backbone.

Octahedron-shaped DNA frames are used in this study to demonstrate the framework assembly on the pattern surface. A DNA octahedron contains twelve 6-helix-bundle edges with an edge length of about 29 nm⁵ (Supplementary Fig. S12). Each frame's vertex features four 30-base protruding single-stranded DNA strands, comprising 22 poly-T bases and an 8-base sequence designed for hybridization (sticky ends). We use a dual-component assembly system comprising two types of DNA frames (denoted as OA and OB, represented in pink and green, respectively, in the schematics throughout the paper) with identical structures and complementary sticky ends at vertices to induce inter-frame hybridization. Inter-frame hybridization between OA and OB, assembly process, and thermal annealing result in two-component crystallization. The initial layer on the surface consists of either one type (just OA) or two types (OA + OB) of DNA frames, which are termed here as a monofunctionalized or bifunctionalized surface, respectively. After the attachment of the initial layer, the nucleation and growth of the 3D lattice at the patterned area is promoted by thermal annealing with the substrates immersed in the mixture of the OA and OB. We have conducted most of the experiments with silicon wafers and demonstrated the adaptability of this approach to different types of oxide surfaces (Fig. 1b).

We demonstrate a successful patterning of DNA frame superlattices over about 10 mm² macroscopic area on a silicon wafer in Fig. 1c, illustrating scalable framework integration over the large areas. Superlattice nucleation is restricted to exposed SiO₂ regions (termed 'growth area'), where the initial layer of frames forms, and is absent in areas where the PEG hydrogel template is present (termed

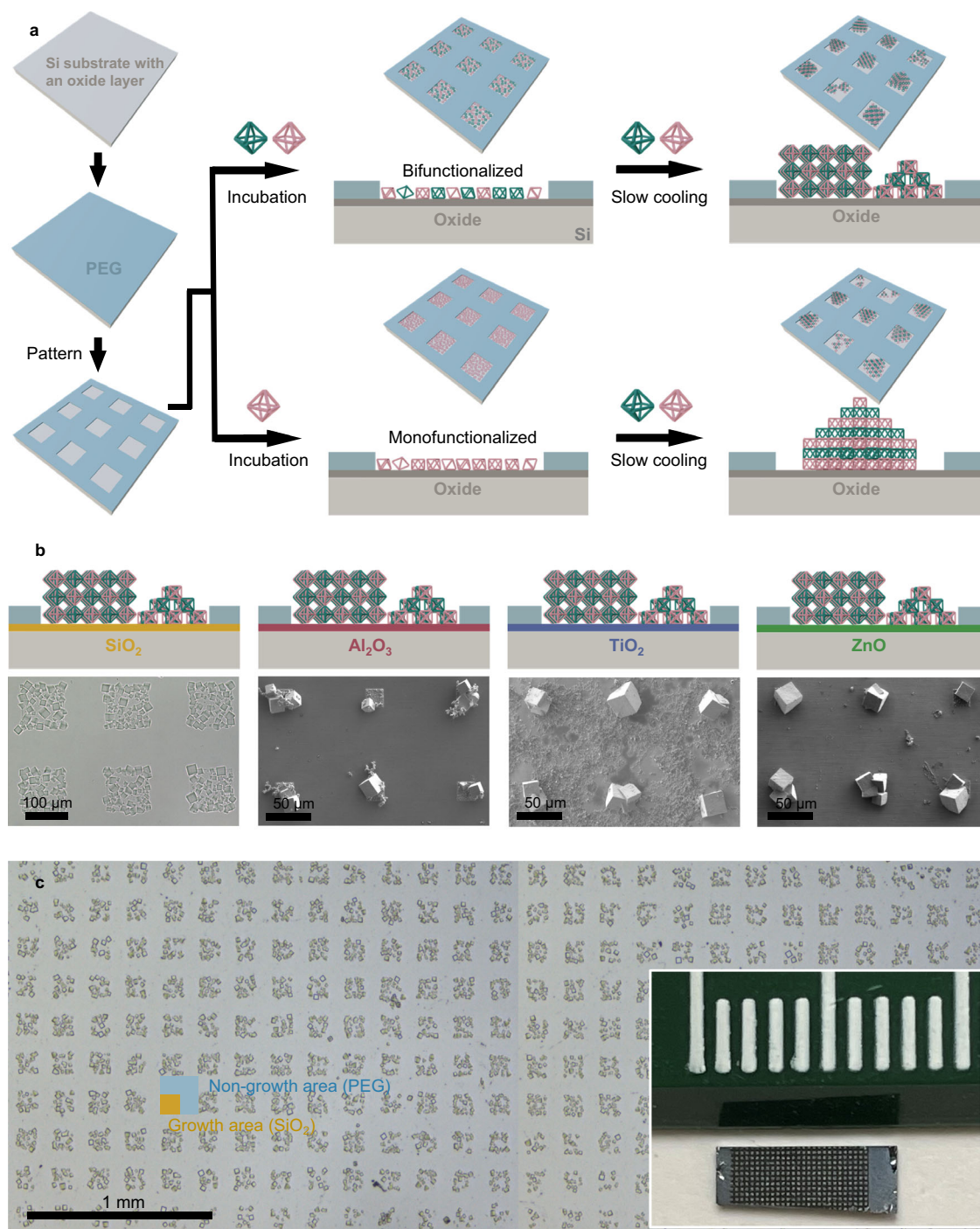


Fig. 1 | Surface-directed patterning of 3D DNA-frame superlattice on oxide surfaces. **a** Schematic illustrating the patterning of PEG template by EBL, followed by the deposition of a layer of octahedral DNA frames, and crystallization of 3D DNA crystals on patterned oxide surfaces with bifunctionalized and monofunctionalized surfaces. **b** Schematics and representation of surface-patterned DNA frame superlattice on bifunctionalized Si/SiO₂, Al₂O₃, TiO₂, and ZnO surfaces, respectively. The edge length of the microwells is 100 μ m for Si/SiO₂ and 20 μ m for

Al₂O₃, TiO₂, and ZnO surfaces. The SiO₂ refers to the native oxide layer on the silicon wafer without additional coating. **c** Optical images showcasing the patterned DNA frame superlattices over a macroscopic area (10 mm²). Field stitches have been utilized to present a larger view. The inset features a photograph of the superlattice-patterned silicon wafer following silication, accompanied by a ruler marked with an overall length of 1 cm for scale reference.

‘non-growth area’). Such superlattice assembly at the liquid-solid interfaces takes place directly on the native oxide layer of the silicon wafer, eliminating the necessity for an additional SiO₂ coating.

We then extended the methodology established for SiO₂ for patterning Al₂O₃, TiO₂, and ZnO surfaces with DNA frame superlattices. Besides silicon oxide, metal oxides often possess suitable electronic⁵² catalytic properties⁵³ and are attractive in biomedical

applications due to their biocompatibility⁵⁴. Similar to SiO₂, the surface of metal oxides in aqueous solutions is hydroxylated due to dissociative chemisorption of water molecules, and the surface hydroxyl groups adsorb ions from the solution by the exchange with hydroxyl protons or hydroxide ions, which leads to surface charges^{55,56}. Our approach successfully patterns these oxide surfaces, as demonstrated in Fig. 1b and Supplementary Figs. S6–S11. This

method is effective because, as long as the pH of the assembly solution is sufficiently higher than the isoelectric point of these surfaces, the surfaces will have a net negative charge, which facilitates the divalent cation bridging of negatively charged DNA frames and enables the formation of superlattices.

Results

To understand the relationship between the initially adsorbed DNA frame layer and the interfacial crystallization process, we investigated the lattice formation for different compositions (one type of frames or dual-frame compositions) of the initially adsorbed layer (Fig. 2). The

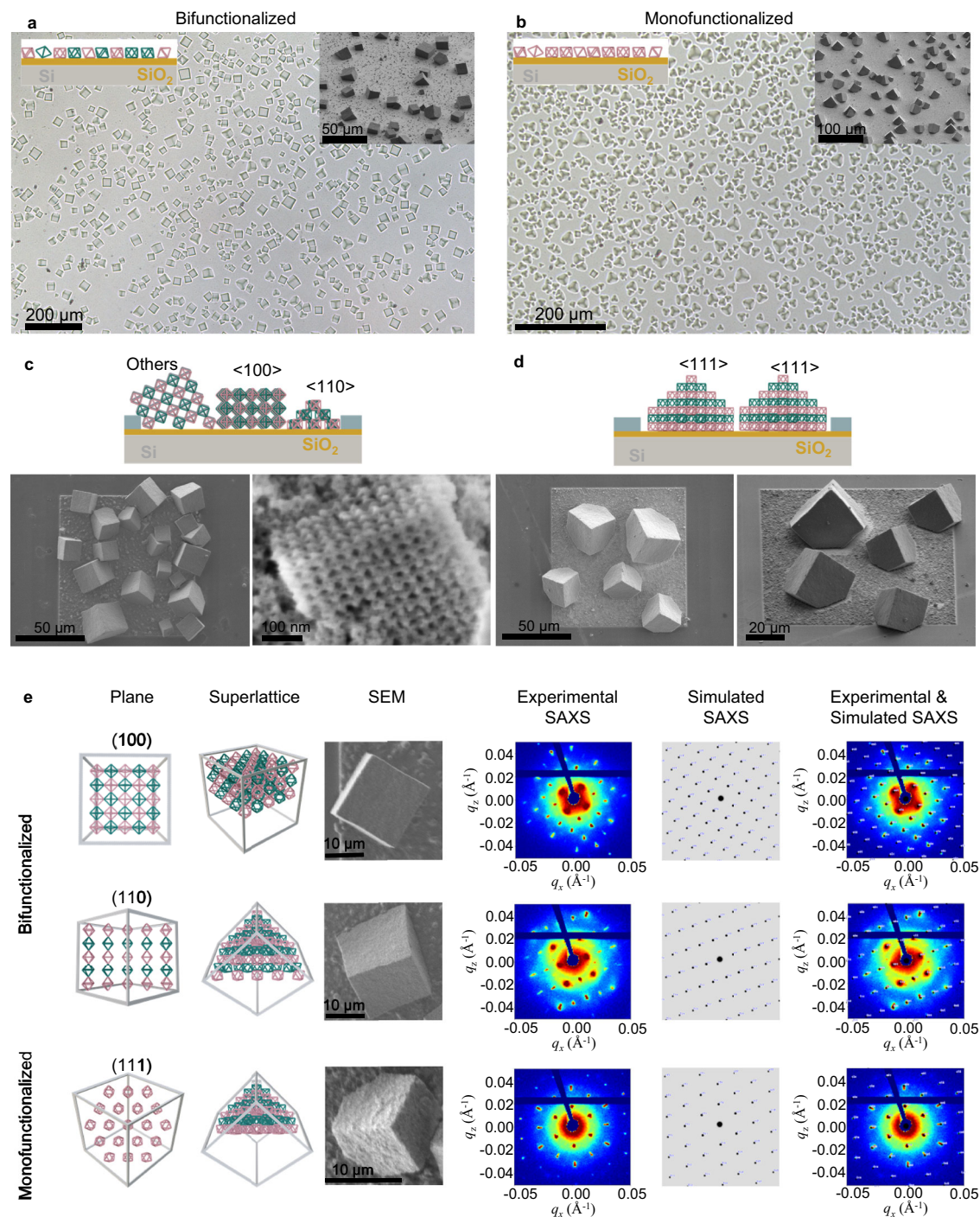


Fig. 2 | Growth of superlattices from DNA frame bifunctionalized and monofunctionalized Si/SiO₂ surfaces. **a** Optical image of DNA frame superlattices on bifunctionalized Si/SiO₂ surface in non-patterned regions. The inset showcases an SEM image of the silicated superlattices. **b** Optical image of DNA origami frame superlattices on monofunctionalized Si/SiO₂ surface in non-patterned regions. The inset showcases an SEM image of the silicated superlattices. **c** Schematic and SEM images illustrating surface-patterned DNA origami frame superlattices on bifunctionalized Si/SiO₂ surface, along with a magnified view of a crystal highlighting the

crystal structures. **d** Schematic and SEM images, including top and side views, of surface-patterned DNA frame superlattices on monofunctionalized Si/SiO₂ surface. **e** DNA frame superlattices grown along different crystallographic orientations from the substrates. Left to Right: Sequentially arranged schematics depicting the (100), (110), and (111) planes from which crystals were grown, schematics of the superlattices, SEM images of the shaped single crystals on the surface, corresponding experimental SAXS data, simulated SAXS data, and an overlay of the experimental SAXS and simulated SAXS data.

initial layer is important in promoting the particular growth plane in the DNA frame superlattice on a surface, as we show below. Our AFM measurements (Supplementary Fig. S31) indicate that DNA octahedral frames have a preferential orientation with their faces against the substrate since this maximizes surface interaction due to the cation bridging. When assembled in bulk, the superlattice formed from octahedral DNA frames, due to their six-fold orthogonal inter-vertex bonds, has a simple cubic (SC) symmetry. The SC single crystal has a Wulff cubic shape, where a cube is enclosed by (100) planes²⁹. Considering the formation of a nucleus on a planar substrate, the crystal can, in principle, nucleate in different orientations with respect to the surface, resulting in cube-shaped crystals truncated at a specific plane that defines the crystals' orientation. The compositions of two origami components vary for different planes of the superlattice. Thus, the orientation of the crystals is dominated by the growth plane of the superlattice in contact with the surface, which is hypothesized to be determined by the initial layer of the DNA frames on the surface. When a cube-shaped two-component crystal with SC symmetry is cut, a large number of the resulting planes contain both OA and OB frames, except for the (111) plane.

To test this hypothesis, we compared the crystal morphology grown on bifunctionalized and monofunctionalized surfaces. Figures 2a, c show the optical images, scanning electron microscopy (SEM) images, and schematic of superlattices that are formed on bifunctionalized substrates, while Fig. 2b, d depict this information for monofunctionalized substrates. Optical images were obtained right after the assembly process, while SEM images were collected after converting the DNA frame superlattice into silica through a sol-gel process⁴⁷ to ensure it was intact under SEM conditions. Indeed, for bifunctionalized substrates, we observed (Fig. 2a, c) that superlattices nucleate and grow with multiple orientations. The shapes of the superlattices on a substrate are derived from its Wulff cubic shape as cubes cut along various planes such as (100) and (110), along with some higher-order planes, which are not necessarily parallel to the cubes' faces or edges. These cutting planes contain both OA and OB frames. For instance, as illustrated in Fig. 2e, both the (100) and (110) planes are composed of OA and OB frames. Although Fig. 2e only shows two planes, there are multiple planes containing both frames; thus, in principle, the superlattices can grow from various planes. In our experiments, high-order planes are often seen on biofunctionalized substrates (Fig. 2a, c, Supplementary Fig. S30). We identified the crystal orientation based on their morphology, as examined by optical microscopy. Of the 766 crystals evaluated in the non-patterned area, 70% exhibited growth from high-order planes, while 16% appeared to be <100> oriented, 10% were <110> oriented, and 4% showed <111> orientation. The detailed cross-sectional analysis (Supplementary Fig. S32) of formed lattices reveals that the first several layers of the crystal at the wafer surface exhibit more defects, but lattice order is mainly recovered after about 5 layers. We attribute the defects within several layers to the disorder in the first layer of DNA frames, whose immobilization on a surface prevents the re-arrangement of frames and transition to order during annealing for these first few layers.

In contrast, when the superlattices were formed on a monofunctionalized substrate (Fig. 2b, d), where only one type of DNA frame is present in the initial surface layer, <111> orientation of growing crystals is promoted, and the cubes are intersected by a (111) plane, consisting of one frame type as shown in the schematic in Fig. 2e. As revealed by the optical and SEM imaging (Fig. 2b, d), almost all the crystallites assembled on a monofunctionalized surface have the same shape and <111> orientation. The substrates are perpendicular to the diagonal of the cubic crystals and meet all six faces of the cubes, leaving a cross-section as a hexagon. The differences in geometry between crystallites formed on bifunctionalized and monofunctionalized surfaces support our hypothesis that the composition of the initial DNA frame layer on the surface has a significant effect on

the growth and lattice orientation for assembly at the liquid-solid interface. To eliminate the possibility that crystals may be assembled in bulk and then fall on surfaces, we incubated the patterned substrates with pre-assembled crystals in TAE/12.5 mM Mg²⁺ buffer. However, we see no adhesion of superlattices to the patterned substrate over days (Supplementary Fig. S18), which confirms that the lattice growth occurs at the solid-liquid interface of the patterned area. We also explored the onset of nucleation for bulk and surface-formed assemblies using in-situ SAXS measurements and observed that the crystallization temperature is slightly higher when lattices are assembled at the surface (Supplementary Fig. S33) for both empty and AuNP-filled frames.

To further investigate the lattice symmetry and orientations of surface-assembled single-crystal domains, we applied a microbeam small-angle X-ray scattering (SAXS) mapping⁵⁷ with a beam size of $5 \times 5 \mu\text{m}^2$ to the surface-patterned crystals, aimed at analyzing the crystals' orientation and morphology previously identified through SEM. This integration of superlattice structures with patterned surfaces permits a multifaceted examination of individual crystals, establishing a correlation between SEM images and SAXS patterns for each crystal. Directing crystallization to patterned surfaces allows us to characterize individual superlattices due to their well-defined placement on surfaces. This is a significant benefit compared to bulk assembly and characterization when only ensemble-averaged information is obtained. In Fig. 2e, we present side-by-side comparisons of SEM images of single crystals with distinct orientations alongside their corresponding SAXS patterns. The SEM images suggest potential <100>, <110>, and <111> orientations of the crystals.

The 2D SAXS patterns of the surface-grown crystals reveal distinct geometries for each orientation, characterized by square, rectangular, and hexagonal arrays corresponding to 4-fold, 2-fold, and 6-fold symmetries, respectively. To further validate these observations, we performed simulations of the SAXS patterns for <100>, <110>, and <111> oriented crystals. These simulations confirm that the X-ray scattering patterns of an SC lattice exhibit specific diffraction patterns depending on the orientation: a square array for the <100> direction, a rectangular array for the <110> direction, and a hexagonal pattern for the <111> direction. The congruence between the experimental SAXS patterns and the simulations underscores our findings. The <100>, <110> oriented crystals grown from bifunctionalized surface, and <111> oriented crystals formed on monofunctionalized surface. On both bifunctionalized and monofunctionalized surfaces, we observed the formation of single crystals, bounded by (100) facets and truncated at various planes, yet preserving the single cubic symmetry. Despite the orientation difference, the lattice constant for these structures after silica embedding measures $51.8 \text{ nm} \pm 0.3 \text{ nm}$. This correlation between SAXS and SEM data provides robust evidence for our structural analysis of the crystal orientations.

Although SAXS identifies the three typical orientations, crystals grown from high-order planes are present on the bifunctionalized surfaces according to the optical and SEM imaging (Fig. 2a, c). Earlier studies¹⁰ on assembling DNA-coated nanoparticles on ssDNA grafted gold surfaces indicated that ssDNA composition affects the crystal orientations, where both monofunctionalized and bifunctionalized surfaces resulted in singular crystal orientations. The observation that bifunctionalized surfaces lead to DNA frame superlattices with diverse orientations may be attributed to variations of the local surface density of the initial layer that can promote the stabilization of planes containing both OA and OB frames at different inter-frame distances.

While the initial layer of origami plays a critical role in determining the superlattice orientation, the microwell size also influences the orientation of the formed crystal (Fig. 3a). From comparing by SEM imaging crystals grown on the nonpatterned area and in arrays of square microwells with edge lengths, a , of 100, 50, and $20 \mu\text{m}$ on a monofunctionalized surface, we conclude that the percentage of

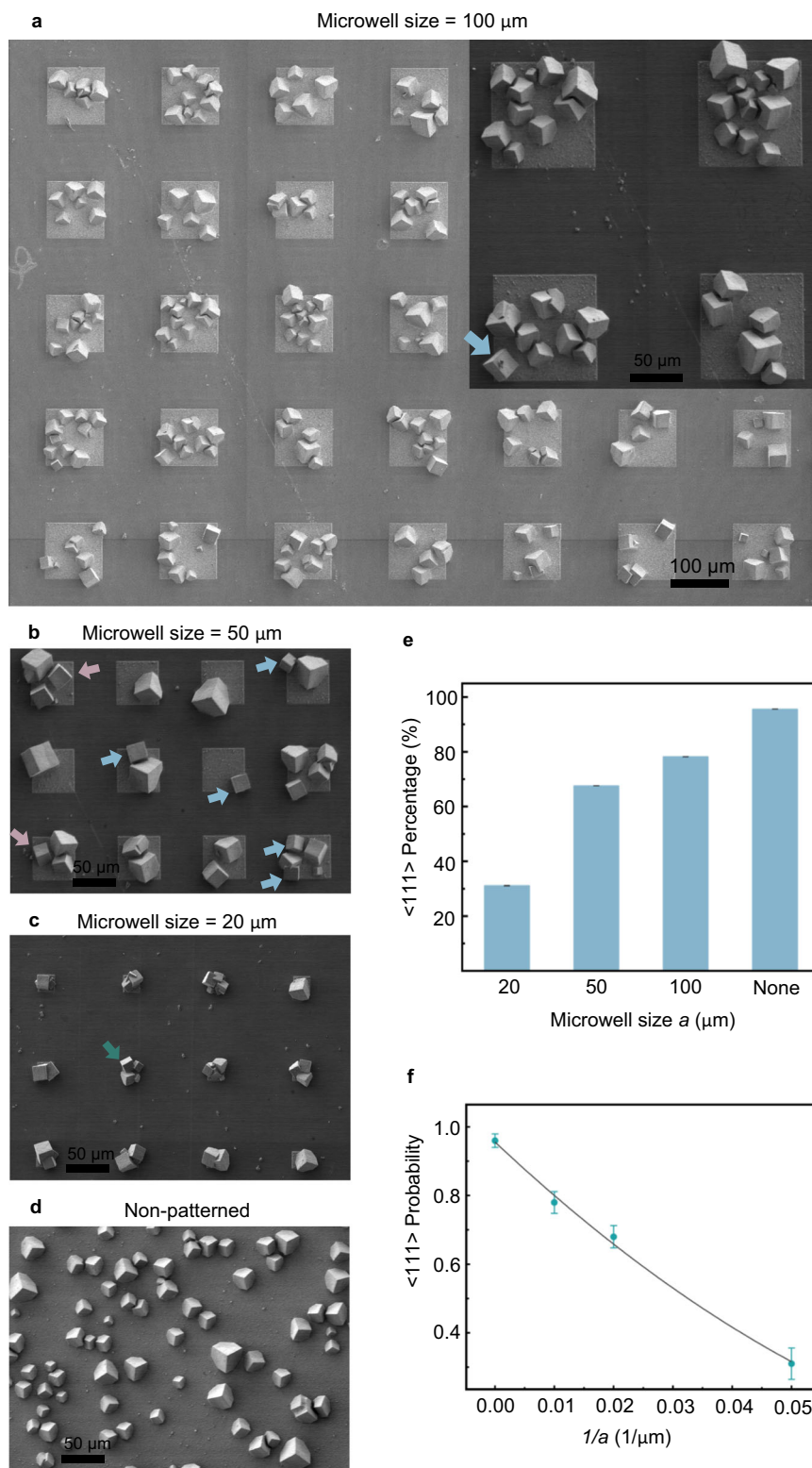


Fig. 3 | Microwell size effect on superlattice surface orientation. **a–d** SEM images illustrating DNA origami frame superlattices grown on patterned monofunctionalized Si/SiO₂ surface in microwell arrays of 100, 50, and 20 μm , alongside a reference image of a non-patterned area. Blue arrows denote crystals deviating from growing along the $\langle 111 \rangle$ direction due to edge effects, pink arrows indicate non- $\langle 111 \rangle$ crystals not located at the edges, and green arrows highlight crystals displaying non- $\langle 111 \rangle$ due to twinning. **e** Histogram showing the percentages of

superlattice grown along the $\langle 111 \rangle$ direction (as obtained for number crystals, N (for different microwell sizes, a), such as N (20 μm) = 148, N (50 μm) = 648, N (100 μm) = 875, N (nonpatterned) = 2520)) in microwell arrays with different sizes and non-patterned area on monofunctionalized Si/SiO₂ surfaces. **f** Probability of $\langle 111 \rangle$ orientation on the inverse of microwell size ($1/a$). Circles represent experimental data, and a line is a model fit to the data.

$\langle 111 \rangle$ oriented superlattice dramatically decreases when a decreases (Fig. 3a–e). On the nonpatterned area, 96% of the cuboid-shaped crystals are $\langle 111 \rangle$ oriented, while the percentage drops to 78, 68, and 31% for superlattices assembled in 100, 50, and 20 μm microwells, respectively (Fig. 3a–e). The dependence of crystal growth orientation on microwell size can be attributed to the presence of edges. Qualitatively, the growth orientation is expected to depend on the edge length per unit growth area or, simply, the inverse of the microwell size ($1/a$). If we hypothesize that the edge effect extends only up to a certain distance and that the growth orientation in the $\langle 111 \rangle$ direction can be described by an average probability within the affected area, then using a simple phenomenological model (see Supporting Information), we find that the probability of preferential growth orientation exhibits a quadratic dependence on a (see Fig. 3f).

Based on this analysis, we found that the edge effect can influence a growth orientation within a zone of up to approximately 4 microns from the edge. We suggest that there are three reasons that preclude $\langle 111 \rangle$ orientation on a monofunctionalized surface, including the edge effect, voids in the first layer, and twinning, while the major effect is caused by the influence of edges and confinement within the microwells. In Fig. 3, examples of the non $\langle 111 \rangle$ oriented crystals grown on a microwell's edge are labeled with blue arrows. Although the exact mechanism is not known, our hypothesis is that the deviation in crystal orientation from the $\langle 111 \rangle$ plane at the edges might primarily be due to the initial adsorption of the DNA origami frames. The initial adsorption is likely influenced by the proximity effects associated with electron beam lithography, which can lead to residual, non-uniform PEG coating and variations in the PEG film thickness at the edges of the microwells. This residual PEG could alter the local surface property, affecting how DNA frames are initially adsorbed. Such surface variations can lead to a heterogeneous nucleation environment, where the DNA frames might not be uniformly distributed during the initial incubation with one type of DNA frame. Our experimental results suggest that while the presence of residual PEG at the edges influences the adsorption of DNA frames at the microwell boundaries, it does not completely prevent their deposition but moderates their surface density. This subtle modulation of adsorption quality could be responsible for the observed deviations in crystal orientation near the edges. For example, the edges of the microwells formed by PEG may not be completely vertical, and this can affect the direction of the DNA frame assembly without suppressing the crystal's growth. Besides, since the microwells are shallow (about the stacking height of 6 to 10 DNA frames), the crystal could grow less constrained and slightly over the edges when wells are filled with frames.

Some of the non $\langle 111 \rangle$ oriented crystals grow in the center of a microwell without touching the edge, as pointed by pink arrows (Fig. 3b). This potentially occurs due to the local distribution of the DNA frames in the initial layer. When there is a void of the absorbed initial layer of frames (Supplementary Fig. S13), both types of DNA frames can bind to the substrates in the subsequent slow cooling step, leading to crystals that are not $\langle 111 \rangle$ oriented. The last scenario is non $\langle 111 \rangle$ oriented crystals with a twinning structure, indicated by green arrows. While drawing clear boundaries between these three cases is challenging, they all share the common consequence that crystals grown on smaller patterns have a higher likelihood of deviating from their intended orientation.

Next, with gained understanding of the importance of the initial layer on lattice assembly at a liquid-solid interface, we investigated the effect of the surface hydrophilicity on the DNA frame interfacial crystallization. The hydrophilicity of the oxide surface reflects a surface charge density, which affects cation bridging and the density of adsorbed DNA frames in the initial layer. From a practical point of view, the hydrophilicity of the oxide surface falls between the two extreme cases: a surface freshly etched in piranha solution and a surface aged in the air for days after etching. Freshly etched wafers have a contact

angle $< 5^\circ$, while for wafers exposed to air, the contact angle of the surface reaches around 30° . The fresh substrates are strongly hydrophilic and have a relatively high charge density due to hydroxyl groups⁵⁸. As a result, such surfaces have a denser initial frame layer due to the larger number of ionic bridges between the surface and DNA backbone. Consequently, higher nucleation density in each square microwell is achieved. In the superlattice growth stage, a densely distributed nucleus on the surface leads to a decrease of local DNA frame concentrations in the surrounding solution, and thus, crystallites with smaller sizes but with high coverage over patterns are formed. On the other hand, the surfaces of silicon wafers become less hydrophilic over time when exposed to air, primarily due to the condensation of silanol groups into siloxane bridges, and the adsorption of organic contaminants from the air. The reduced surface charge affects the surface density of DNA frames in the initial layer, thus leading to lower nucleation density and lower surface coverage but larger crystal sizes (Fig. 4a, b).

We characterized surface coverage (a ratio of areas covered by crystals to the area of microwell) by optical microscopy and analyzed the data, as detailed in the supplementary information. The coverage can exceed 100% if crystals grow over the microwell edge. Under the same annealing protocol for 100 μm and 20 μm microwells, the coverages of crystals on freshly etched surfaces are $87 \pm 8\%$ and $254 \pm 34\%$, respectively, while on aged surfaces they are $26 \pm 13\%$ and $122 \pm 109\%$, respectively. The particularly large error bar for aged 20 μm well indicates a strong surface heterogeneity, which is more critical for smaller microwells. At the same time, the sizes of crystals on freshly etched surfaces are less than half the size of those on aged surfaces, with $10.2 \pm 2.2 \mu\text{m}$ and $25.1 \pm 9.4 \mu\text{m}$ correspondingly in 100 μm microwells (Fig. 4c). The number of crystal domains on hydrophilic surfaces is 90 ± 9 per 100 μm microwell and 9 ± 2 per 20 μm well, while on aged surfaces is 4 ± 4 per 100 μm microwell and 2 ± 2 per 20 μm microwell. Thus, these observations support our hypothesis that surface coverage is decreased on aged surfaces compared to freshly etched surfaces due to the reduced affinity and, as a result, the suppressed nucleation density.

To enhance control and fine-tune surface coverage, we studied how the passivation of surfaces with DNA frames without sticky ends (inactive frames, OT) affects surface coverage and domain size. We prepared surfaces with an initial layer consisting of the three types of origami frames (OA, OB, and OT): OA and OB can hybridize with each other (active) and OT is the inactive one that has poly-T as extruding ends and thus cannot hybridize with the other two DNA frames. We observed that when the inactive DNA frames are at a comparable concentration to the active ones at the initial attachment step, the crystal coverage is reduced compared to the case of only active origami frames present (Supplementary Fig. S17). We concluded that the passivation of surface inactivated frames has a similar effect, as decreasing surface hydrophilicity, in reducing surface coverage of crystals since the inactive frames do not provide hybridization for the next layer, and consequently, lattice growth is inhibited.

For fresh surfaces, we explored how pattern design affects crystal growth by altering the ratio between the exposed oxide surface of microwells and the PEG-protected area between microwells, and specifically, through changes in microwell sizes and spacing between them in the pattern. We designed microwell arrays with well sizes of 10, 20, and 100 μm , and center-to-center spacings of 100, 100, and 200 μm , respectively. This design allows us to probe the ratio of non-growth areas to growth areas (A_n/A_g) of a pattern, as defined in Fig. 1c, and compare this to unpatterned areas where the non-growth area is zero. The respective ratios are 99, 24, and 3 for the 10, 20, and 100 μm microwell sizes (Supplementary Fig. S15). By examining the areas for twinning crystals, we identify three different growth regimes for twinning corresponding to zero non-growth area ratio ($A_n/A_g = 0$), low non-growth area ratio ($A_n/A_g \sim 3$), and high non-growth area ratios

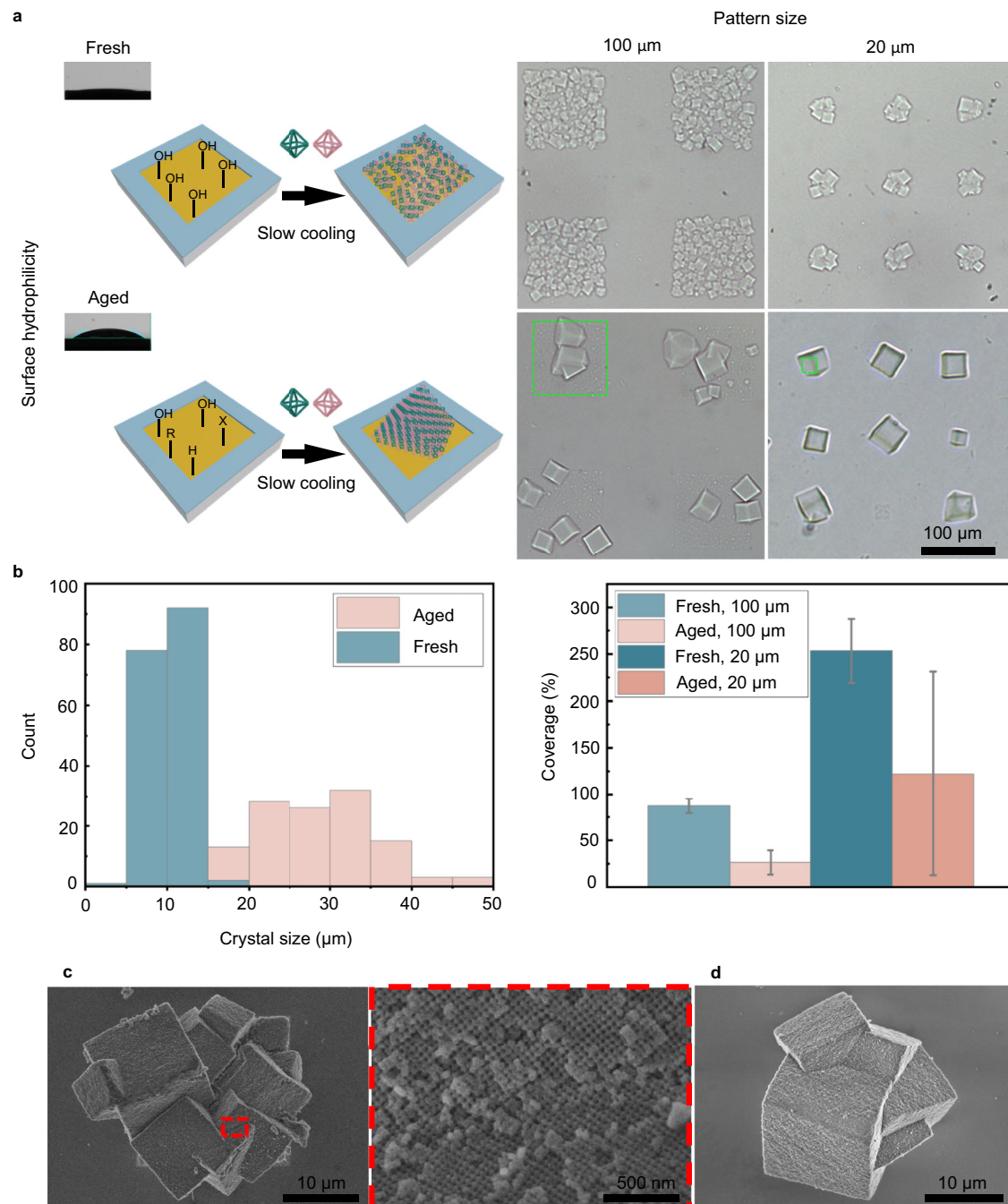


Fig. 4 | Effect of surface hydrophilicity and microwell size on crystal growth. **a** Schematic and optical images of DNA frame superlattice grown on piranha solution freshly treated silicon wafers or aged silicon wafers (exposed to air for days after piranha solution etching) with 100 μm and 20 μm microwell arrays (In both cases, DNA frame concentration was 150 nM). The top-left images are water contact angle measurements of the silicon wafers. The microwells were outlined with green

dash lines. **b** Histogram of crystal sizes ($N = 151\text{--}173$) and the percentages of surface coverage of crystals over microwells ($N = 39\text{--}99$) on freshly etched vs aged silicon wafers. **c** Representation of crystals grown in a microwell array with 20 μm size and 100 μm spacing on freshly etched surfaces. **d** Representation of crystals grown in a microwell array with 10 μm microwell and 100 μm spacing on freshly etched surfaces.

(An/Ag; $>$ - 24). For these three cases, we see a trend of increasing twinning for each growth regime as the non-growth to growth area increases (Figs. 2a, 4c, d, Supplementary Figs. S20–22). As nucleation progresses, DNA frame concentration might be depleted near the growing crystal, with the magnitude of the effect depending on the pattern size and spacing. For the high ratios of non-growth to growth areas (patterns with smaller microwells), there is less DNA frame depletion, and therefore, a lattice rate growth is higher. This can result in the observed formation of twin boundaries for smaller microwells.

Building on our understanding of lattice assembly at the solid-patterned interface, we sought to overcome the depletion of DNA frames during the thermal annealing process by exploring secondary growth on surface-bound crystals that act as seeds. This seed-mediated approach in the superlattice assembly process permits enhancing coverage of microwells and increases the crystal sizes. The fact that DNA frame superlattice assembles at the temperature below lattice melting makes it possible to realize re-growth without melting previously formed crystals. Secondary growth occurs when fresh DNA

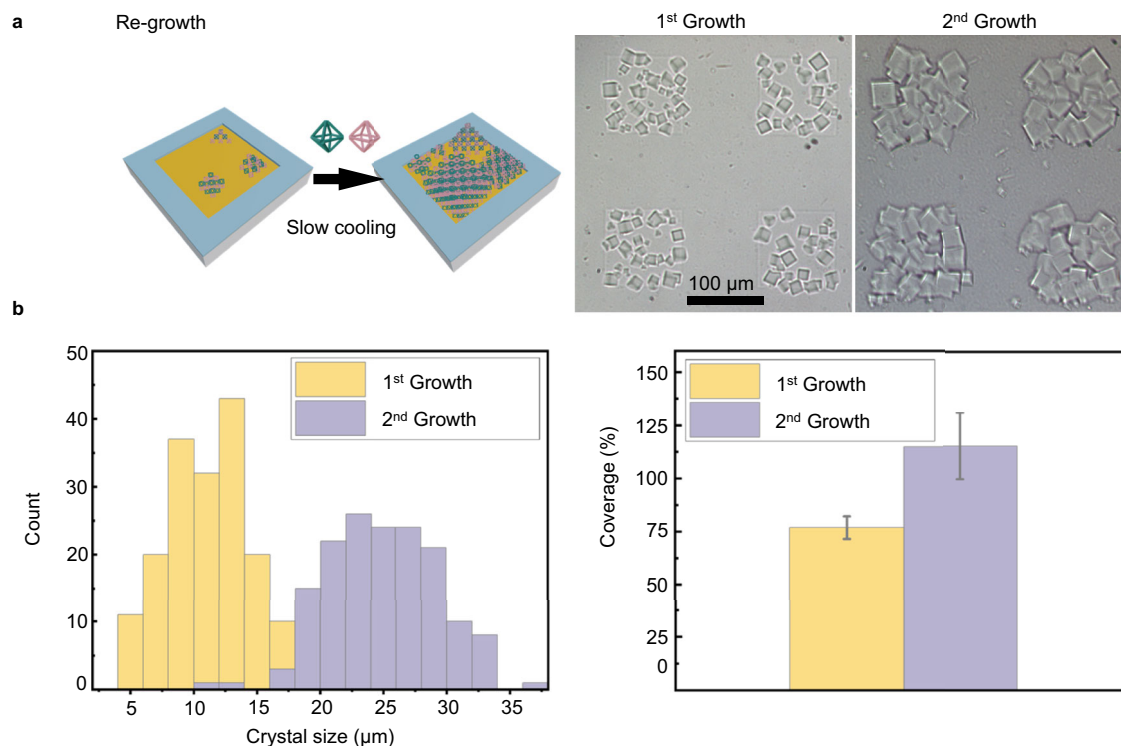


Fig. 5 | Re-growth of surface-patterned superlattice. **a** Schematic and optical microscopy images of DNA frame superlattice patterned on 100 μm microwell arrays after 1st growth and 2nd growth (DNA frame concentration was 100 nM for

1st growth and 150 nM for the 2nd growth). **b** Histogram of crystal sizes ($N = 156\text{--}177$) and the percentages of surface coverage of crystals over microwells ($N = 34\text{--}38$) after 1st growth and 2nd growth.

frames are added and slowly cooled from a temperature of 42 °C, which is lower than the crystal melting temperature (43 °C), to room temperature. This secondary growth over the seeds leads to larger crystallites and the formation of new nuclei in empty places of a pattern (Fig. 5a and Supplementary Figs. S24). The optical microscopy analysis of the re-growth process shows that the surface coverage of lattices in the 100 μm microwell increases from $77 \pm 5\%$ after 1st growth (100 nM origami frames) to $115 \pm 16\%$ 2nd growth, meanwhile, the crystal sizes increased from $11.3 \pm 3.5 \mu\text{m}$ to $25.0 \pm 4.3 \mu\text{m}$ (Fig. 5b). The histogram in Fig. 5b compares the distribution of crystal sizes after 1st growth and 2nd growth, respectively. After the 2nd growth, the distribution of the crystal sizes gets broader.

Our approach for assembling DNA frame lattices onto pre-patterned surfaces can be scaled up to create complex, arbitrarily shaped patterns, as demonstrated in Fig. 6. For example, Fig. 6a displays a pattern designed in the likeness of a smiley face, spanning an area over 400 μm in diameter and consisting of crystal arrays configured into curvilinear contours and ovals. This capability to fabricate arbitrarily shaped 3D superlattices is significant for potential device integration. Our patterning technique's scalability is showcased in the depiction of the Brookhaven National Laboratory logo, which extends over 4 mm in Fig. 6a, demonstrating the viability of this method for fabricating large-area, intricate patterns at the millimeter scale. This advance opens new possibilities for the integration of DNA-based assemblies into a variety of surface-engineered materials and devices.

Beyond creating 3D superlattices using DNA frames, we broaden the application of this approach to produce surface-patterned arrays containing precisely placed nano-cargos. Gold nanoparticles (AuNPs) with a diameter of 10 nm are functionalized with DNA and can be incorporated into DNA frames through DNA hybridization. Similarly, Alexa488 labeled streptavidin molecules can be loaded into DNA frames. Upon mixing DNA frames, nano-cargos (AuNPs or Alexa488-streptavidins) with the pre-patterned substrates, and annealing, 3D

nano-cargo arrays are formed into pre-defined shapes on substrates. Figure 6b shows the patterning of AuNPs superlattice into a dog shape and microwell arrays with different numbers of crystals per microwell. The red color of the pattern in comparison to the transparent superlattices in optical images when they are empty indicates the successful incorporation of AuNPs into the DNA frame superlattice. The ability to incorporate proteins in 3D frameworks patterned onto the surface is illustrated in Fig. 6c, where a Columbia University Engineering School logo image is formed by patterned fluorescent 3D arrays of Alexa488-streptavidin. The successful incorporation of Alexa488-streptavidin into the DNA framework gives rise to the fluorescent signal. This modification is significant as nano-cargos often contribute to the unique properties and functionalities inherent in the superlattice structure. Our approach enables functional nano-objects like plasmonic nanoparticles (for example, AuNPs) and proteins (for example, streptavidin) to be used as nano-cargos within frames and their arrays and distributed in customized designed locations on substrates (Fig. 6b, c), which is important for downstream applications such as biosensors, photonic devices, electronic devices.

In summary, we have demonstrated the methodology for directing assembly of 3D DNA programmable superlattices on planar surfaces over macroscopic areas by patterning a monolayer of DNA frames on surfaces. The approach is applicable to a variety of oxide surfaces without using any surface-specific chemical functionalization. We investigated the orientation, size, and coverage of the crystals that can be controlled, as we show, by surface properties, annealing processes, and pattern design. Thus, a robust surface pattern-guided 3D assembly method was established. The established approach provides a adaptable platform to systematically study the nucleation and growth of DNA-based assemblies at the interfaces. This method also enables potent control over the directing the growth of 3D DNA framework assemblies on substrates in arbitrarily manner over macroscopic areas, which can be further used in the optical, mechanical, electronic and biomaterial applications.

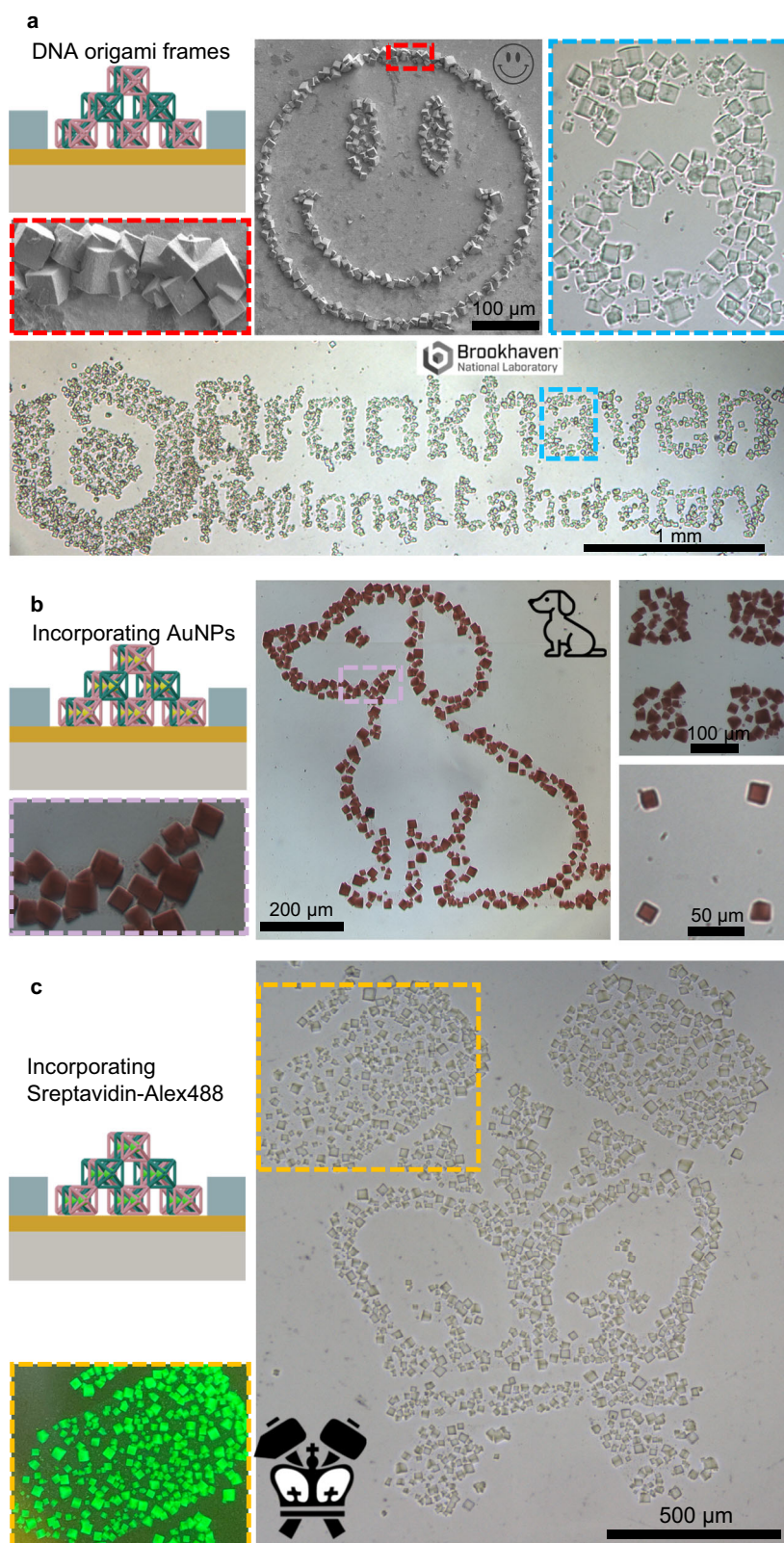


Fig. 6 | Surface patterned DNA frame superlattices in arbitrarily shaped patterns and with incorporated nano-cargos. **a** SEM image of a DNA frame superlattice patterned as a smiley face on bifunctionalized Si/SiO₂ surfaces. Optical microscopy images of DNA frame superlattice patterned as Brookhaven National Laboratory logo across millimeter scales. **b** Optical images of DNA frame

superlattice incorporated with AuNPs (10 nm in diameter) patterned as a dog cartoon and in 100 μ m, 10 μ m microwell arrays. **c** Optical images of DNA frame superlattice encaged with Alexa 488 labeled streptavidin patterned as the logo of Columbia University Engineering School.

Methods

Substrate preparation

Single-crystal silicon wafers (Type: P (Boron), Orientation: <100>, 1 primary flat, 5 mm × 5 mm or 5 mm × 7 mm, Ted Pella) were cleaned with piranha solution (3:1 mixture of concentrated sulfuric acid and 30% hydrogen peroxide; exercise caution) overnight. After piranha solution etching, the silicon wafers were washed with deionized (DI) water multiple times and kept in DI water for further use. Prior to use, these substrates were dried by flowing air gun and exposed to oxygen plasma at 20 W, 100 mTorr for 10 min.

Atomic layer deposition (ALD) of TiO₂, Al₂O₃ and ZnO

TiO₂, Al₂O₃, and ZnO coatings were applied onto silicon wafers in a Cambridge Nanotech Savannah S100 atomic layer deposition (ALD) system. TiO₂ was deposited using vapors of titanium isopropoxide (preheated to 80 °C) and water as precursors, carried by a nitrogen gas flow of 20 sccm. The substrate temperature was maintained at 120 °C. The thickness of the TiO₂ film was determined at 104.0 ± 0.1 Å, after 246 ALD cycles. Similarly, the Al₂O₃ deposition was achieved under identical conditions as TiO₂ deposition, except for utilizing trimethylaluminum and water vapors as precursors. The thickness of the Al₂O₃ coating reached 129.6 ± 0.1 Å after 100 ALD cycles. ZnO coatings followed the same procedures, employing diethylzinc and water vapor as precursors. The thickness of ZnO reached 105.9 ± 0.1 Å after 40 ALD cycles. For all cases, the film thickness was determined with a J.A. Woollam M-2000 Spectroscopic Ellipsometer.

Surface patterning

Surface patterned hydrogel templates were fabricated on silicon wafers via previously established methods with slight modifications^{50,51}. Contiguous PEG thin films, ~50 nm thick, were spin-cast onto these substrates using a 2 wt% precursor solution of biotinylated poly(ethylene glycol) (Biotin-PEG-Biotin, M_w = 5 kDa) or methoxy (CH₃O)-capped polyethylene glycol with one hydroxyl group (mPEG-OH, M_w = 5 kDa) in tetrahydrofuran (THF). Biotinylated PEG was employed as the e-beam resist for all samples, except for the superlattice containing streptavidin-Alexa488, where mPEG-OH was utilized. JEOL JBX-6300FS electron beam lithography (EBL) system was used for patterning. A typical exposure is done with 100 keV incident electron energy, a beam current of 25 nA, shot spacing of 40 nm. For silicon wafers without any coating, 200 μC/cm² electron dose was used. For Al₂O₃, ZnO or TiO₂-coated silicon wafers, 400 μC/cm² electron dose was used. In this case, hydrogel templates with controllable sizes and spacings are created. After electron exposure, the specimens were rinsed with DI water 3 times to remove un-crosslinked PEG.

Preparation of octahedral DNA frames

Octahedral DNA frames were prepared by mixing 20 nM of M13mp18 scaffold DNA and 100 nM of each staple oligonucleotides in 1 × TAE buffer containing 12.5 mM MgCl₂ (TAE/MgCl₂). The mixed solution was gradually cooled from 90 °C to room temperature over a period of 20 h to induce the folding of the DNA. Subsequently, DNA frames were purified using the Amicon centrifugal filter units (100 kDa, Millipore Sigma) and centrifuged at 2000 × g and at 4 °C. Purification was repeated 5 times by adding fresh TAE/MgCl₂ buffer in each cycle. The design and DNA sequences of the octahedral DNA frames are provided in Supplementary Information. Each octahedron origami frame contains twelve 6-helix-bundle edges with an edge length of about 29 nm⁵. Each vertex of the octahedral-shaped frames has 4 single-stranded DNA sticking out, which are 30 bases long and include 22 bases of poly T and 8 bases of sequences for hybridization (sticky ends).

DNA functionalization of nano-cargos

Gold nanoparticles. Thiolated DNA (Integrated DNA Technologies, IDT) were first reduced by tris[2-carboxyethyl] phosphine (TCEP) in

H₂O at 1: 100 ratio and then purified by a size exclusion column (G-25, GE Healthcare). Spherical AuNPs with a diameter of ~10 nm (Ted Pella Inc.) was then mixed with the DNA in a ratio of 1:300, followed by adding buffer to obtain 10 mM phosphate buffer (pH 7) after 2 h. Following buffer addition, sodium chloride solution was slowly added into the mixture until a final concentration of 0.3 M was reached. The solution was then aged at room temperature for at least 12 h. Excessive reagents were removed by centrifuging the solution 6 times and washing with 10 mM phosphate buffer with 100 mM sodium chloride. **Streptavidin.** A solution of streptavidin-Alexa488 conjugate (Sigma Aldrich) was mixed with biotinylated DNA (IDT) at a ratio of 1:4 and incubated overnight in the dark to prepare DNA functionalized streptavidin-Alexa488.

Self-assembly of DNA frame superlattice on patterned substrates

Patterned substrates were cut to 2.5 mm × 5 mm or 2.5 mm × 7 mm sizes before putting into the solution of DNA frames. For bifunctionalized surfaces, the assembly on substrates was achieved in one step as substrates were put into the mixture of two types of empty frame superlattices (OA and OB) and was incubated for 30 min at 50 °C before cooled from 50 °C to room temperature at a rate of 0.1 °C/30 min. The two types of DNA frames with complementary sticky ends were mixed in a 1:1 ratio. Superlattice grown on monofunctionalized surfaces were fabricated through a two-step process, where substrates were incubated with one type of DNA frame (OA) solution at 50 °C overnight, then transferred to the mixture of two types of DNA frames before slowing cooling from 50 °C to room temperature. For DNA frame superlattice with DNA functionalized nano-cargos (gold nanoparticles or streptavidin-Alexa488) inside, the nano-cargos were mixed with DNA frames at a 1:1.2 ratio for AuNPs and 1:1.15 for streptavidin-Alexa488.

Silica embedding process

N-trimethoxysilylpropyl-N, N, N-trimethylammonium chloride (TMSPA, Gelest, 50% in methanol) was added to in 1 mL of TAE buffer containing 12.5 mM MgCl₂ and was vigorously mixed. The substrate with superlattice was transferred into the solution and left on the bench at room temperature for over 16 h. Then triethoxysilane (TEOS, Gelest) was added, and the sample sat on the bench for an additional 24 to 48 hrs. The substrates were then rinsed in DI water and ethanol and allowed to air dry.

Optical and electron microscopy

Optical images of patterned superlattice in buffer were captured with Eclipse Ti2 inverted microscope. SEM images of silicate superlattice on patterned surfaces were acquired using a Hitachi 4800 field emission SEM.

Small-angle X-ray scattering (SAXS)

The SAXS experiments were performed at the Life Science X-ray Scattering (LiX, 16-ID) and the Complex Materials Scattering (CMS, 11-BM) beamlines at the National Synchrotron Light source II (NSLS-II) at Brookhaven National Laboratory. The sample substrates placed vertically were illuminated by a horizontal incident X-ray beam in the transmission mode.

Data availability

The additional data supporting the findings of this study are available within this article and its Supplementary Information and from the corresponding author upon request. Source data are provided in this paper.

References

1. Liu, W. et al. Diamond family of nanoparticle superlattices. *Science* **351**, 582–586 (2016).

2. Zhang, T. et al. 3D DNA Origami Crystals. *Adv. Mater.* **30**, 1800273 (2018).
3. Laramy, C. R., O'Brien, M. N. & Mirkin, C. A. Crystal engineering with DNA. *Nat. Rev. Mater.* **4**, 201–224 (2019).
4. Hong, F., Zhang, F., Liu, Y. & Yan, H. DNA Origami: Scaffolds for creating higher order structures. *Chem. Rev.* **117**, 12584–12640 (2017).
5. Tian, Y. et al. Ordered three-dimensional nanomaterials using DNA-prescribed and valence-controlled material voxels. *Nat. Mater.* **19**, 789–796 (2020).
6. Kahn, J. S. & Gang, O. Designer nanomaterials through programmable assembly. *Angewandte Chem.* **61**, e202105678 (2022).
7. Posnjak, G. et al. Diamond-lattice photonic crystals assembled from DNA origami. *Science* **384**, 781–785 (2024).
8. Wickham, S. F. J. et al. Complex multicomponent patterns rendered on a 3D DNA-barrel pegboard. *Nat. Commun.* **11**, 5768 (2020).
9. Xin, Y. et al. Scaling up DNA origami lattice assembly. *Chem. Eur. J.* **27**, 8564–8571 (2021).
10. Lewis, D. J., Zornberg, L. Z., Carter, D. J. D. & Macfarlane, R. J. Single-crystal winterbottom constructions of nanoparticle superlattices. *Nat. Mater.* **19**, 719–724 (2020).
11. Zornberg, L. Z. et al. Self-assembling systems for optical out-of-plane coupling devices. *ACS Nano* **17**, 3394–3400 (2023).
12. Du, J. S., Bae, Y. & De Yoreo, J. J. Non-classical crystallization in soft and organic materials. *Nat. Rev. Mater.* **9**, 229–248 (2024).
13. Chen, J. et al. Building two-dimensional materials one row at a time: Avoiding the nucleation barrier. *Science* **362**, 1135–1139 (2018).
14. Penzo, E., Wang, R., Palma, M. & Wind, S. J. Selective placement of DNA origami on substrates patterned by nanoimprint lithography. *J. Vac. Sci. Technol. B* **29**, 06F205 (2011).
15. Hung, A. M. et al. Large-area spatially ordered arrays of gold nanoparticles directed by lithographically confined DNA origami. *Nat. Nanotechnol.* **5**, 121–126 (2010).
16. Kershner, R. J. et al. Placement and orientation of individual DNA shapes on lithographically patterned surfaces. *Nat. Nanotechnol.* **4**, 557–561 (2009).
17. Martynenko, I. V. et al. Site-directed placement of three-dimensional DNA origami. *Nat. Nanotechnol.* **18**, 1456–1462 (2023).
18. Gopinath, A. et al. Absolute and arbitrary orientation of single-molecule shapes. *Science* **371**, eabd6179 (2021).
19. Gopinath, A., Miyazono, E., Faraon, A. & Rothmund, P. W. Engineering and mapping nanocavity emission via precision placement of DNA origami. *Nature* **535**, 401–405 (2016).
20. Shetty, R. M., Brady, S. R., Rothmund, P. W. K., Hariadi, R. F. & Gopinath, A. Bench-top fabrication of single-molecule nanoarrays by DNA origami placement. *ACS Nano* **15**, 11441–11450 (2021).
21. Gopinath, A. & Rothmund, P. W. K. Optimized assembly and covalent coupling of single-molecule DNA origami nanoarrays. *ACS Nano* **8**, 12030–12040 (2014).
22. Scheible, M. B., Pardatscher, G., Kuzyk, A. & Simmel, F. C. Single molecule characterization of DNA binding and strand displacement reactions on lithographic DNA origami microarrays. *Nano Lett.* **14**, 1627–1633 (2014).
23. Chen, C. et al. Ultrafast dense DNA functionalization of quantum dots and rods for scalable 2D array fabrication with nanoscale precision. *Sci. Adv.* **9**, eadh8508 (2023).
24. Xin, Y., Martinez Rivadeneira, S., Grundmeier, G., Castro, M. & Keller, A. Self-assembly of highly ordered DNA origami lattices at solid-liquid interfaces by controlling cation binding and exchange. *Nano Res.* **13**, 3142–3150 (2020).
25. Kielar, C., Ramakrishnan, S., Fricke, S., Grundmeier, G. & Keller, A. Dynamics of DNA origami lattice formation at solid-liquid interfaces. *ACS Appl. Mater. Interfaces* **10**, 44844–44853 (2018).
26. Meyer, R., Sacca, B. & Niemeyer, C. M. Site-directed, on-surface assembly of DNA nanostructures. *Angew. Chem. Int. Ed. Engl.* **54**, 12039–12043 (2015).
27. Bashar, S. et al. Coverage percentage and coverage rate of different DNA nanostructures grown on a mica substrate. *Curr. Appl. Phys.* **15**, 1358–1363 (2015).
28. Woo, S. & Rothmund, P. W. Self-assembly of two-dimensional DNA origami lattices using cation-controlled surface diffusion. *Nat. Commun.* **5**, 4889 (2014).
29. Aghebat Rafat, A., Pirzer, T., Scheible, M. B., Kostina, A. & Simmel, F. C. Surface-assisted large-scale ordering of DNA origami tiles. *Angew. Chem. Int. Ed. Engl.* **53**, 7665–7668 (2014).
30. Suzuki, Y., Kawamata, I., Watanabe, K. & Mano, E. Lipid bilayer-assisted dynamic self-assembly of hexagonal DNA origami blocks into monolayer crystalline structures with designed geometries. *iScience* **25**, 104292 (2022).
31. Suzuki, Y., Endo, M. & Sugiyama, H. Lipid-bilayer-assisted two-dimensional self-assembly of DNA origami nanostructures. *Nat. Commun.* **6**, 8052 (2015).
32. Lee, J. et al. Coverage control of DNA crystals grown by silica assistance. *Angew. Chem. Int. Ed. Engl.* **50**, 9145–9149 (2011).
33. Tapio, K. et al. Large-scale formation of DNA origami lattices on silicon. *Chem. Mater.* **35**, 1961–1971 (2023).
34. Aissaoui, N. et al. Free-standing DNA origami superlattice to facilitate cryo-EM visualization of membrane vesicles. *J. Am. Chem. Soc.* **146**, 12925–12932 (2024).
35. Gabrys, P. A. & Macfarlane, R. J. Controlling crystal texture in programmable atom equivalent thin films. *ACS Nano* **13**, 8452–8460 (2019).
36. Wang, M. X. et al. Epitaxy: Programmable atom equivalents versus atoms. *ACS Nano* **11**, 180–185 (2017).
37. Hellstrom, S. L. et al. Epitaxial growth of DNA-assembled nanoparticle superlattices on patterned substrates. *Nano Lett.* **13**, 6084–6090 (2013).
38. Estephan, Z. G., Qian, Z., Lee, D., Crocker, J. C. & Park, S.-J. Responsive multidomain free-standing films of gold nanoparticles assembled by DNA-directed layer-by-layer approach. *Nano Lett.* **13**, 4449–4455 (2013).
39. Choi, J., Kim, J., Park, J.-y., Hyun, J. K. & Park, S.-J. Domain-selective enzymatic cross-linking and etching for shape-morphing DNA-linked nanoparticle films. *Nano Lett.* **24**, 2574–2580 (2024).
40. Lewis, D. J., Carter, D. J. D. & Macfarlane, R. J. Using DNA to control the mechanical response of nanoparticle superlattices. *J. Am. Chem. Soc.* **142**, 19181–19188 (2020).
41. Zheng, C. Y. et al. Confined growth of DNA-assembled superlattice films. *ACS Nano* **16**, 4813–4822 (2022).
42. Wong, A. M. et al. Arrays of colloidal single crystals engineered with DNA in lithographically defined microwells. *Nano Lett.* **23**, 116–123 (2023).
43. Hueckel, T., Lewis, D. J., Mertiri, A., Carter, D. J. D. & Macfarlane, R. J. Controlling colloidal crystal nucleation and growth with photolithographically defined templates. *ACS Nano* **17**, 22121–22128 (2023).
44. Sun, L. et al. Position- and orientation-controlled growth of wulff-shaped colloidal crystals engineered with DNA. *Adv. Mater.* **32**, e2005316 (2020).
45. Gavrilović, S., Brüggenthies, G. A., Weck, J. M., Heuer-Jungemann, A. & Schwille, P. Protein-assisted large-scale assembly and differential patterning of DNA origami lattices. *Small* **20**, 2309680 (2024).
46. Wang, S. T. et al. Designed and biologically active protein lattices. *Nat. Commun.* **12**, 3702 (2021).
47. Majewski, P. W. et al. Resilient three-dimensional ordered architectures assembled from nanoparticles by DNA. *Sci. Adv.* **7**, eabf0617 (2021).
48. Michelson, A. et al. Three-dimensional nanoscale metal, metal oxide, and semiconductor frameworks through DNA-programmable assembly and templating. *Sci. Adv.* **10**, eadl0604 (2024).

49. Jing, X. et al. Solidifying framework nucleic acids with silica. *Nat. Protoc.* **14**, 2416–2436 (2019).
50. Teng, F. & Libera, M. Microlens enhancement of surface-tethered molecular beacons. *Langmuir* **34**, 14969–14974 (2018).
51. Krsko, P., Sukhishvili, S., Mansfield, M., Clancy, R. & Libera, M. Electron-beam surface-patterned poly(ethylene glycol) micro-hydrogels. *Langmuir* **19**, 5618–5625 (2003).
52. Yu, X., Marks, T. J. & Facchetti, A. Metal oxides for optoelectronic applications. *Nat. Mater.* **15**, 383–396 (2016).
53. Li, D. et al. Induced activation of the commercial Cu/ZnO/Al₂O₃ catalyst for the steam reforming of methanol. *Nat. Catal.* **5**, 99–108 (2022).
54. Solanki, P. R., Kaushik, A., Agrawal, V. V. & Malhotra, B. D. Nanostructured metal oxide-based biosensors. *NPG Asia Mater.* **3**, 17–24 (2011).
55. Tamura, H., Tanaka, A., Mita, K.-y & Furuichi, R. Surface hydroxyl site densities on metal oxides as a measure for the ion-exchange capacity. *J. Colloid Interface Sci.* **209**, 225–231 (1999).
56. Szekeres, M. & Tombácz, E. Surface charge characterization of metal oxides by potentiometric acid–base titration, revisited theory and experiment. *Colloids Surf. A: Physicochem. Eng. Asp.* **414**, 302–313 (2012).
57. Yang, L., Liu, J., Chodankar, S., Antonelli, S. & DiFabio, J. Scanning structural mapping at the Life Science X-ray Scattering Beamline. *J. Synchrotron Radiat.* **29**, 540–548 (2022).
58. Yang, X. M., Zhong, Z. W., Diallo, E. M., Wang, Z. H. & Yue, W. S. Silicon wafer wettability and aging behaviors: Impact on gold thin-film morphology. *Mater. Sci. Semicon. Process.* **26**, 25–32 (2014).

Acknowledgements

We thank A. Michelson for the helpful suggestions. The work was supported by the US Department of Energy, Office of Basic Energy Sciences, grant DE-SC0008772. This research used the Materials Synthesis & Characterization, Nanofabrication, Advanced Optical Spectroscopy and Microscopy, and Electron Microscopy facilities of the Center for Functional Nanomaterials, which are US DOE Office of Science Facilities at Brookhaven National Laboratory under contract no. DE-SC0012704. This research also used the Complex Materials Scattering (CMS, 11-BM) and the Life Science X-ray Scattering (LiX, 16-ID) beamlines of the National Synchrotron Light Source II, a U.S. Department of Energy (DOE) Office of Science User Facility operated for the DOE Office of Science by Brookhaven National Laboratory under Contract No. DE-SC0012704. The LiX beamline is part of the Center for BioMolecular Structure (CBMS), which is primarily supported by the National Institutes of Health, National Institute of General Medical Sciences (NIGMS) through a P30 Grant (P30GM133893), and by the DOE Office of Biological and Environmental Research (KP1605010). LiX also received additional support from NIH Grant S10 OD012331. The AFM study of surface-adsorbed DNA frames was supported by the U.S. Department of Energy (DOE), Office of Science, Office of Basic Energy Sciences (BES), as part of the Energy Frontier Research Centers program: CSSAS, The Center for the Science of Synthesis Across Scales under Award Number DE-SC0019288. PNNL

is a multi-program national laboratory operated for DOE by Battelle under Contract No. DE-AC05-76RL01830.

Author contributions

F.T. and O.G. conceived concepts and designed the experiments. F.T. performed the experiments. H.Z., R.L., L.Y., and D.N. contributed to SAXS measurements and analysis. D.N. contributed to the modeling of <111> probability and AFM of surface patterned hydrogels. N.T. provided training to F.T. in EBL and facilitated discussions on optimizing EBL processes. Z.X. and M.L. conducted ALD. M.H. contributed to the calculation of surface coverage through optical images. S.Z. and F.T. conducted the AFM measurements of the DNA frames on the surface. F.T. and O.G. wrote the manuscript. All authors discussed the results and commented on the manuscript.

Competing interests

The authors declare no competing interests.

Additional information

Supplementary information The online version contains supplementary material available at <https://doi.org/10.1038/s41467-025-58422-0>.

Correspondence and requests for materials should be addressed to Oleg Gang.

Peer review information *Nature Communications* thanks the anonymous reviewer(s) for their contribution to the peer review of this work. A peer review file is available.

Reprints and permissions information is available at <http://www.nature.com/reprints>

Publisher's note Springer Nature remains neutral with regard to jurisdictional claims in published maps and institutional affiliations.

Open Access This article is licensed under a Creative Commons Attribution-NonCommercial-NoDerivatives 4.0 International License, which permits any non-commercial use, sharing, distribution and reproduction in any medium or format, as long as you give appropriate credit to the original author(s) and the source, provide a link to the Creative Commons licence, and indicate if you modified the licensed material. You do not have permission under this licence to share adapted material derived from this article or parts of it. The images or other third party material in this article are included in the article's Creative Commons licence, unless indicated otherwise in a credit line to the material. If material is not included in the article's Creative Commons licence and your intended use is not permitted by statutory regulation or exceeds the permitted use, you will need to obtain permission directly from the copyright holder. To view a copy of this licence, visit <http://creativecommons.org/licenses/by-nc-nd/4.0/>.

© The Author(s) 2025